CrossMark

Four Sub-Earth Planets Orbiting Barnard's Star from MAROON-X and ESPRESSO

Ritvik Basant[1] , Rafael Luque[1,5] , Jacob L. Bean[1] , Andreas Seifahrt[2] , Madison Brady[1] , Lily L. Zhao[1,5] ,
Nina Brown[1] , Tanya Das[1] , Julian Stürmer[3] , David Kasper[1] , Rohan Gupta[1] , and Guðmundur Stefánsson[4]

[1] Department of Astronomy & Astrophysics, University of Chicago, Chicago, IL 60637, USA; rbasant@uchicago.edu
[2] Gemini Observatory/NSF NOIRLab, 670 N. A'ohoku Place, Hilo, HI 96720, USA
[3] Landessternwarte, Zentrum für Astronomie der Universität Heidelberg, Königstuhl 12, D-69117 Heidelberg, Germany
[4] Anton Pannekoek Institute for Astronomy, University of Amsterdam, Science Park 904, 1098 XH Amsterdam, The Netherlands

Abstract

Barnard's Star is an old, single M dwarf star that comprises the second-closest extrasolar system. It has a long history of claimed planet detections from both radial velocities and astrometry. However, none of these claimed detections have so far withstood further scrutiny. Continuing this story, extreme precision radial velocity measurements from the ESPRESSO instrument have recently been used to identify four new sub-Earth-mass planet candidates around Barnard's Star. We present here 112 radial velocities of Barnard's Star from the MAROON-X instrument that were obtained independently to search for planets around this compelling object. The data have a typical precision of $30\,\mathrm{cm\,s^{-1}}$ and are contemporaneous with the published ESPRESSO measurements (2021–2023). The MAROON-X data on their own confirm planet b ($P = 3.154$ days) and planet candidates c and d ($P = 4.124$ and 2.340 days, respectively). Furthermore, adding the MAROON-X data to the ESPRESSO data strengthens the evidence for planet candidate e ($P = 6.739$ days), thus leading to its confirmation. The signals from all four planets are $<50\,\mathrm{cm\,s^{-1}}$, the minimum masses of the planets range from 0.19 to $0.34\,M_\oplus$, and the system is among the most compact known among late M dwarfs hosting low-mass planets. The current data rule out planets with masses $>0.57\,M_\oplus$ (with a 99% detection probability) in Barnard's Star's habitable zone ($P = 10$–42 days).

Unified Astronomy Thesaurus concepts: Exoplanets (498); Radial velocity (1332); Spectroscopy (1558)

1. Introduction

At a distance of only 1.83 pc (Gaia Collaboration et al. 2021), Barnard's Star is a touchstone for studies of nearby stars. It is a single, mid–M dwarf star that is notable for having the largest proper motion of any star in the sky. Barnard's Star is thought to be ∼10 Gyr old due to its slow rotation and low levels of activity (see discussions in B. Gauza et al. 2015 and K. France et al. 2020). An up-to-date summary of Barnard's Star's properties can be found in Table 1 of J. I. González Hernández et al. (2024). Note that another common name for Barnard's Star is Gl 699 (W. Gliese 1957).

Recently, radial velocity observations using the extreme precision radial velocity (EPRV) spectrograph ESPRESSO on the Very Large Telescope (VLT; F. Pepe et al. 2021) have revealed four very low-mass planet candidates in close-in orbits ($P = 2$–7 days) around Barnard's Star (J. I. González Hernández et al. 2024). The detected signals have semiamplitudes that range from 47 down to $20\,\mathrm{cm\,s^{-1}}$, and they represent some of the smallest radial velocity signals claimed to date. J. I. González Hernández et al. (2024) were confident enough to declare the signal at $P = 3.154$ days as due to a bona fide planet ("Barnard b"), but they left the other signals as planet candidates.

Due to its nearness and low mass, Barnard's Star has been the subject of many searches for planets. Although there have been claims of planet detections using both astrometry and radial velocities dating back decades, none of the previous claimed detections survived additional observations and analyses (G. D. Gatewood 1995; G. F. Benedict et al. 1999; J. Lubin et al. 2021; É. Artigau et al. 2022). In an attempt to confirm and measure the radius of Barnard b, A. K. Stefanov et al. (2025) looked for transits in TESS data, but they did not detect any transit signals.

In this Letter, we present an extensive set of radial velocity measurements of Barnard's Star from the MAROON-X instrument on Gemini-N. MAROON-X is an EPRV spectrograph with a wavelength coverage (500–920 nm) optimized for M dwarfs like Barnard's Star (A. Seifahrt et al. 2016, 2018, 2020, 2022). We describe our MAROON-X observations and data reduction in Section 2. We present analyses of the MAROON-X and ESPRESSO data that confirm and extend the results of J. I. González Hernández et al. (2024) in Section 3. We conclude with a discussion in Section 4.

2. Observations and Data Reduction

We have been observing Barnard's Star with MAROON-X regularly since 2021 because it is a key target of our ongoing search for planets around stars within 4 pc. We have previously published results from our 4 pc planet search for Wolf 359 and Teegarden's Star (R. Bowens-Rubin et al. 2023; S. Dreizler et al. 2024). We observed Barnard's Star as a regular science target and we also observed it as a calibration target to validate the performance of MAROON-X for other programs. The data presented in this Letter cover three seasons from 2021 to 2023. MAROON-X was used in campaign mode during this period, with discrete observing runs ranging from 1 to 5 weeks in duration. The Barnard's Star observations we analyze here were obtained during nine distinct observing runs.

---

[5] NHFP Sagan Fellow.

All the MAROON-X observations of Barnard's Star were 5 minute exposures, and most visits comprised just a single exposure. Barnard's Star is so bright for Gemini+MAROON-X that we mostly observed it in mid- to below-average conditions (i.e., 85th percentile image quality and 70th percentile cloud cover were typical constraints). We even occasionally observed it in very poor conditions as part of Gemini's "Band 4" time (i.e., heavy cloud cover and/or bad seeing). These poor weather observations typically had multiple successive exposures because otherwise, the telescope would have been idle. All the individual exposures were reduced separately. We discarded seven exposures that were taken in particularly bad observing conditions and thus have anomalously low signal to noise. We then binned the radial velocity values for observations taken within 60 minutes. The total data set used here is based on 151 individual exposures obtained over 112 unique epochs.

We reduced and extracted wavelength-calibrated 1D spectra from Barnard's Star data using our standard pipeline, which was first used for radial velocity measurements and described by T. Trifonov et al. (2021) and J. G. Winters et al. (2022). We measured radial velocities from the reduced spectra using a specific version of the serval package (M. Zechmeister et al. 2018) that was modified to work with MAROON-X data. The serval code uses a template-matching approach where the observed spectrum with the highest signal-to-noise ratio (SNR) is chosen as a reference. The remaining spectra are shifted to this reference frame and then serval coadds them to produce a high-SNR template. The template-matching approach for computing radial velocities is more suitable for the rich spectra of M dwarfs than cross-correlation with binary templates. The telluric mask provided within serval was manually checked against a spectrum of an extremely fast rotating ($v \sin i \sim 100 \, \mathrm{km \, s^{-1}}$) A0-type star obtained via MAROON-X in fairly wet conditions for Maunakea (precipitable water vapor $\sim$5 mm) at 1.5 air mass. This custom mask contains all lines deeper than 1% and is not dependent on air mass or precipitable water vapor.

In addition to radial velocities, serval measures various activity indicators, including the chromatic, differential line width, Hα, Ca II triplet, and Na I doublet indices. MAROON-X has two arms, "Blue" ($\lambda = 500$–670 nm) and "Red" ($\lambda = 650$–920 nm), which are reduced and analyzed separately. We used the barycorrpy code (S. Kanodia & J. Wright 2018) to calculate the barycentric correction, including the effect of secular acceleration. The barycentric Earth radial velocities for the MAROON-X observations range from -24.825 to $+26.526 \, \mathrm{km \, s^{-1}}$. The radial velocities are given in Table 4 in the Appendix.

MAROON-X has been using a passively stabilized Fabry–Pérot etalon (J. Stürmer et al. 2017) as the primary calibration source since its first light. Simultaneous etalon spectra are obtained using a dedicated fiber during each science exposure. The simultaneous etalon spectra are used to measure the drift of the instrument from reference etalon spectra taken through the science fibers during daytime calibrations. The etalon parameters were determined once in 2020 by comparison to a ThAr reference spectrum. The etalon is observed to drift at the low level of $2 \, \mathrm{cm \, s^{-1}}$ per day based on comparison with ThAr spectra taken between 2021 August and 2023 October (R. Basant et al. 2025). As described in the next section, we correct this drift using free offsets between observing runs

rather than applying a correction from the ThAr data or from the ensemble approach of R. Basant et al. (2025).

The reduced MAROON-X spectra for Barnard's Star have a peak SNR of 176 and 460 per pixel in the wavelength ranges of 633–643 and 800–812 nm for the Blue and Red arms, respectively. The median radial velocity errors from serval are $37 \, \mathrm{cm \, s^{-1}}$ for Blue arm data and $29 \, \mathrm{cm \, s^{-1}}$ for Red arm data. For comparison, the ESPRESSO data from J. I. González Hernández et al. (2024) have median errors of $10 \, \mathrm{cm \, s^{-1}}$ based on spectra taken with three times longer exposures (15 minutes versus our 5 minutes) and utilizing the full wavelength range of the data. Taking the weighted mean of our Blue and Red arm data and dividing the error by $\sqrt{3}$ gives $13 \, \mathrm{cm \, s^{-1}}$, which provides a comparison to the ESPRESSO precision. MAROON-X's throughput is lower than ESPRESSO's, partially due to a smaller fiber entrance on the sky ($0\rlap{.}''77$ versus $1\rlap{.}''0$), and we rarely observed Barnard's Star in good conditions. ESPRESSO also has a higher spectral resolution ($R \sim 138{,}000$ versus $85{,}000$), which is an advantage for radial velocity measurements. However, MAROON-X has a redder wavelength coverage (red cutoff of 920 versus 788 nm) that is better for M dwarfs (A. Reiners & M. Zechmeister 2020).

3. Methods and Results

3.1. Modeling Stellar Activity

Besides a long-term magnetic activity cycle with $P \sim 3800$ days (B. Toledo-Padrón et al. 2019), radial velocities of Barnard's Star exhibit activity-induced variation at both the rotational period ($\sim$142 days) and its second harmonic ($\sim$71 days, J. I. González Hernández et al. 2024). Such stellar activity-induced radial velocity variations not only produce statistically significant signals in the periodograms (D. Queloz et al. 2001) but also pose a significant challenge in characterizing sub-m s^{-1} signals (D. A. Fischer et al. 2016).

Gaussian processes (GPs) have been proven to be an efficient way to mitigate the effects of stellar activity in the radial velocity data (see, e.g., V. Rajpaul et al. 2015). J. I. González Hernández et al. (2024) performed a detailed analysis of the activity-induced variations in Barnard's Star radial velocities by modeling them simultaneously along with the FWHM of the cross-correlation function (CCF). The authors concluded that a double simple harmonic oscillator (DSHO) kernel, centered on the rotational period and its second harmonic, can effectively model the activity signals in data for Barnard's Star.

For an initial test, we compute the generalized Lomb–Scargle (GLS) periodogram (M. Zechmeister & M. Kürster 2009) of the raw MAROON-X radial velocities (shown in the top panel of Figure 6 in the Appendix), provided via PyAstronomy (S. Czesla et al. 2019). The raw radial velocities exhibit periodic signals associated with the stellar rotation period ($\sim$142 days; J. I. González Hernández et al. 2024). Moreover, a prominent signal near the edge of the frequency grid ($\sim$600 days) is observed, which we associate with the MAROON-X instrumental drift.

As an additional diagnostic, we computed periodograms for the spectroscopic activity indicators, including the chromatic index, differential line width, and Hα index (see the bottom panels of Figure 6 in the Appendix). The chromatic index measures the correlation between the radial velocities and wavelength, while the differential line width characterizes

width changes in individual line profiles, serving as an analog to the FWHM in the cross-correlation technique. The periodogram of the chromatic index from the Red channel data of MAROON-X exhibits significant signals around both the stellar rotation period and its second harmonic. Similarly, the periodogram of the differential line width from the Red channel data of MAROON-X shows significant signals around the second harmonic of the rotation period, within the error bars. Although the differential line width of the Blue channel in the MAROON-X data exhibits similar trends, the chromatic index does not. We attribute this difference to the variation in signal-to-noise between the two arms; the Red arm data are twice as precise as the Blue arm data due to differing amounts of radial velocity information content in the respective spectra for this red star.

Consequently, as our analysis of the stellar activity is consistent with the results presented in J. I. González Hernández et al. (2024), we decided to adopt a DSHO GP kernel. We use `juliet` (N. Espinoza et al. 2019), a versatile modeling tool that builds upon `RadVel` (B. J. Fulton et al. 2018), to model the radial velocity data. The `juliet` code employs `dynesty` (J. S. Speagle 2020) to perform nested sampling and estimates the (log-)marginal likelihood ($\ln Z$), a useful statistical measure to compare models.

The DSHO GP kernel, available within `juliet` via `celerite2` (D. Foreman-Mackey et al. 2017; D. Foreman--Mackey 2018), is parameterized by $\sigma_{\mathrm{GP-INST}}$ (standard deviation of the data), P_{rot} (rotational period of the primary oscillator), Q_0 (quality factor for the second oscillator), f (ratio of amplitudes of the secondary and the primary mode), and last, dQ (the difference between the quality factors of both oscillators). We note that we do not use a 2D GP model as was done by J. I. González Hernández et al. (2024), but instead we only model the radial velocities. Although much simpler, it can still accurately recover the planet parameters (well within 1σ) derived by J. I. González Hernández et al. (2024) for both the 1-Planet and 4-Planet models (see Figure 8 in the Appendix).

In addition to the GP model, we also model an additional white noise (jitter) term (σ) in the radial velocity data. Last, we elected to use free offsets (γ) between the MAROON-X observing runs because this approach has proven highly effective for probing short-period ($P \lesssim 15$ days) planets like the Barnard's Star candidates. For example, MAROON-X data with free run offsets have been used to measure the velocity semiamplitudes of close-in TESS planets to 10 cm s^{-1} or better (e.g., J. A. Caballero et al. 2022; M. Brady et al. 2024). Repeating the analysis with run offsets constrained by an ensemble analysis of many MAROON-X targets R. Basant et al. (2025) gives similar results.

GP models are very flexible, which could lead to data overfitting. To prevent this, we use a normal prior on the rotation period hyperparameter (P_{rot}) of the GP with the mean 142 days and standard deviation 9 days as derived in J. I. González Hernández et al. (2024). We use a uniform prior ($\mathcal{U}$ [0, 1]) on hyperparameter f and a log-uniform prior $\mathcal{LU}$ [0.1, 100]) on both Q_0 and dQ. We share the GP hyperparameters f, dQ, Q_0, and P_{rot} across different runs because of two reasons: (1) these hyperparameters are related to the time-dependent properties of the oscillator and are less likely to be wavelength-dependent for radial velocity signals caused by stellar surface inhomogeneities, and (2) sharing these

hyperparameters between runs helps in more efficient mitigation of the stellar activity thanks to the longer baseline to constrain these characteristic parameters. The GP hyperparameter $\sigma_{\mathrm{GP-INST}}$ is directly related to the amplitude of the radial velocity signal imprinted by the stellar activity and is, therefore, wavelength-dependent (N. Huélamo et al. 2008; A. Reiners et al. 2010; C. J. Crockett et al. 2012). Therefore, we chose not to share $\sigma_{\mathrm{GP-INST}}$ between different instruments but only between multiple data sets from the same instrument. It is assigned a uniform prior $\mathcal{U}$ [0, 10].

3.2. Independent Detection of Planets b, c, and d Using MAROON-X

We first analyzed the MAROON-X data on their own to provide an independent assessment of the planet candidates proposed by J. I. González Hernández et al. (2024). We focused our primary analyses on the Red arm data from MAROON-X because they are potentially less influenced by stellar activity. The results are all consistent or even better (e.g., higher marginal evidence and smaller parameter uncertainties) when including the Blue arm data. Figures showing the results of analyses of the Blue arm data (Figures 10, 11, 12, and 13) can be found in the Appendix. Ultimately, we find that the root mean square (RMS) of the residuals is about twice as large in the Blue arm data compared to the Red arm data despite the photon-limited errors only being 27% larger.

The second panel of Figure 1 shows the residuals after removing the GP model from the MAROON-X Red channel radial velocities. The periodogram shows two significant signals (false alarm probability (FAP) > 0.1%) at the locations of planet b and candidate d, and a third signal (FAP > 1%) at the location of planet candidate c.

To characterize these signals, we follow an iterative strategy. Once we identify a significant signal having FAP > 0.1%, we model it in the radial velocity data using a Keplerian orbit. We then compute the residuals and recompute the periodogram. In the case of multiple significant signals, we model only one of them and check if the other signals still appear in the periodogram and then repeat this process for all other signals. We keep adding additional Keplerian signals until the periodogram of the residuals does not show any significant signals. We ran similar models multiple times to analyze possible variances in the marginal evidence. Finally, following R. Trotta (2008), we confirm a signal originating from an orbiting planet if the improvement in the marginal evidence is >5.0.

The periodograms with successive planets removed are shown in Figure 1. The periodograms show multiple high-frequency signals with FAP $\gtrsim$ 1% in addition to those we identify as due to planets. We associate them with the following aliases of the planetary signals: 0.70 days (1-day alias of 2.34 day signal), 0.41 days (1-day alias of 0.70 day signal), 1.75 days (1-day alias of 2.34 day signal), 1.46 days (1-day alias of 3.15 day signal), 1.32 days (1-day alias of 4.12 day signal), and 0.80 days (1-day alias of 4.12 day signal).

The Keplerian orbits in `juliet` were parameterized using orbital period (P), velocity semiamplitude (K), and time of periastron passage (t_0). Given the high computational cost associated with modeling a large number of parameters, we decided to use a uniform prior on the planetary period with a width of 0.1 days centered around the values estimated via periodogram analysis. Furthermore, as the semiamplitudes for all four planet candidates around Barnard's Star are less than
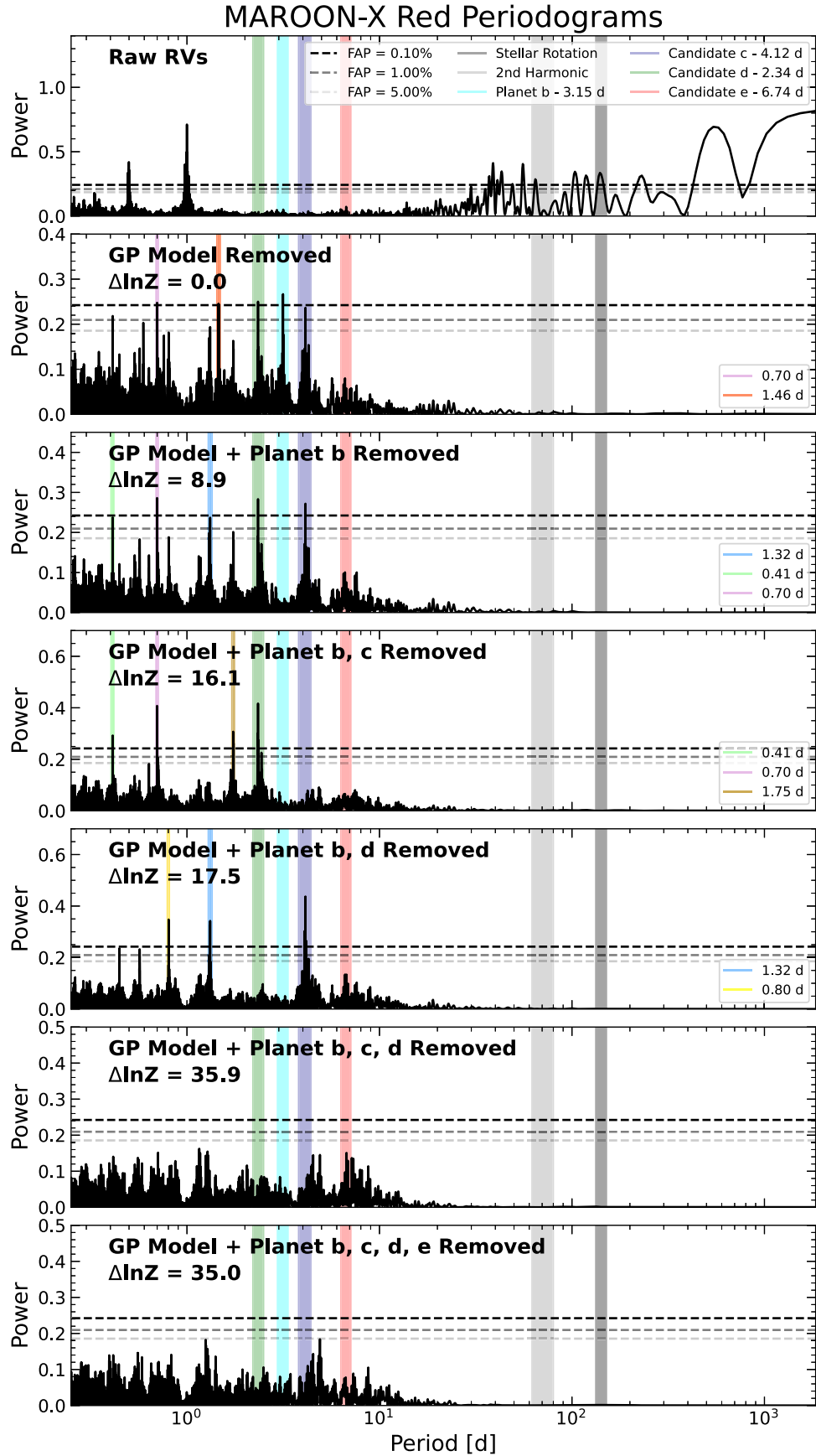
Figure 1. This plot shows the computed GLS periodograms for the residuals of MAROON-X Red channel radial velocities. A β distribution for the planetary eccentricities has been used for all the planets.

Table 1
This Table Summarizes the Marginal Evidence for Different Models Fitted to
the MAROON-X Red Channel Radial Velocities

Model	$\ln Z$	$\Delta \ln Z$
GP-only model	−183.5	0
Circular orbit		
1-Planet (b)	−174.1	9.4
2-Planet (b, c)	−169.6	14.0
2-Planet (b, d)	−164.3	19.2
3-Planet (b, c, d)	−147.9	35.6
β prior on eccentricity		
1-Planet (b)	−174.6	8.9
2-Planet (b, c)	−167.5	16.1
2-Planet (b, d)	−166.1	17.5
3-Planet (b, c, d)	**−147.6**	**35.9**
4-Planet (b, c, d, e)	−148.5	35.0
Uninformative prior on eccentricity		
1-Planet (b)	−176.7	6.9
2-Planet (b, c)	−169.5	14
2-Planet (b, d)	−166.7	16.9
3-Planet (b, c, d)	−144.6	38.9

Note. The 3-Planet model assuming the β prior on the eccentricities (bold) is
the preferred fit to these data.

Table 2
This Table Summarizes the Change in Marginal Evidence between Different
Models for the MAROON-X Red Channel + ESPRESSO Data Assuming the
β Prior on the Eccentricities

Model	$\ln Z$	$\Delta \ln Z$
Global GP		
GP-only model	−412.3	0
1-Planet (b)	−386.6	25.7
2-Planet (b, d)	−365.2	47.1
3-Planet (b, c, d)	−333.7	78.6
4-Planet (b, c, d, e)	−326.4	85.9
Instrument-by-instrument GP		
GP-only model	−419.8	0
1-Planet (b)	−393.0	26.8
2-Planet (b, d)	−370.3	49.5
3-Planet (b, c, d)	−332.8	87.0
4-Planet (b, c, d, e)	**−325.6**	**94.3**

Note. The 4-Planet model using instrument-by-instrument GP (bold) is the
preferred fit to these data.

$\sim 0.5\,\mathrm{m\,s^{-1}}$, we used a uniform prior on semiamplitude $\mathcal{U}$
$[0, 2]\,\mathrm{m\,s^{-1}}$.

To select the best parameterization for the eccentricities, we
tested three different scenarios: (1) parameterizing the
eccentricities as $h = \sqrt{e}\sin\omega$ and $k = \sqrt{e}\cos\omega$ and using
an uninformative uniform prior $\mathcal{U}$ $[−1, 1]$ on both these
parameters; (2) drawing eccentricities directly from a β
distribution β $[1.52, 29]$ and drawing the argument of
periastron (ω) from a uniform distribution $\mathcal{U}$ $[−180, 180]$ (this
eccentricity distribution is well suited for systems with multiple
transiting planets; V. Van Eylen et al. 2019); and last, (3)
assuming circular orbits.

The results of these tests are presented in Table 1. In all
cases, the marginal evidence improves by >5.0 over the
previous model. However, our use of uninformative prior on
the eccentricity parameters h and k results in high-eccentricity
solutions ($0.10^{+0.12}_{-0.07}$ for planet b, $0.24^{+0.11}_{-0.11}$ for planet c, and
$0.44^{+0.09}_{-0.10}$ for planet d), which likely arise due to the low signal
to noise of the data. Such high-eccentricity solutions yield
marginal evidences that are comparable to the low-eccentricity
solutions (e.g., eccentricities drawn from a β distribution).
Additionally, such high eccentricities will likely make the
system unstable (see Section 3.4). Drawing eccentricities
directly from a β distribution forces the eccentricities to be
low, which is typical for compact multiplanet systems (V. Van
Eylen et al. 2019), while still exploring high-eccentricity
solutions. Moreover, unlike the case of circular orbits, this
parameterization of eccentricity preserves some information
about the possible eccentricities of these planets. Therefore, we
decided to draw eccentricities from a β $[1.52, 29]$ distribution
and the argument of periastron from a uniform $\mathcal{U}$ $[−180, 180]$
distribution for all models used in the remainder of this Letter.

We began by modeling the most significant signal at
3.154 days, which corresponds to planet b. Once this signal

is modeled and removed from the radial velocity data, the
periodogram of the residuals shows two significant signals at
the locations of planet candidates c ($P = 4.124$ days) and d
($P = 2.340$ days, see the third panel in Figure 1). Additionally,
for the 1-Planet model, the marginal evidence improves
significantly over the GP-only model by 8.9.

We then modeled both of the additional signals, one by one.
The periodograms of the residuals of the 2-Planet models each
show the third, unmodeled signal (shown in the fourth and fifth
panels of Figure 1). Irrespective of the order in which the
second planet is added, the marginal evidence of the 2-Planet
model improves significantly over the 1-Planet model (see
Table 1).

Finally, we added a third Keplerian signal in our model. We
ran this model 5 times to analyze any variance in marginal
evidence. The $\ln Z$ ranges from $[−149.7, −146.2]$ with a
median and standard deviation of $−147.6 \pm 1.2$. Although the
posteriors for all runs are consistent, the runs with the lowest
$\ln Z$ have a few samples drawn around the 1 yr aliases of
planets c and d. We identify this as the main source of variance
in $\ln Z$. We report the median values of $\ln Z$ in Table 1 and in
Figure 1, while we chose the model that has evidence closest to
the median $\ln Z$ as our final model. For the 3-Planet model, the
marginal evidence increases significantly, improving by 35.9
compared to the GP-only model, and by 18.4 and 19.8 relative
to the 2-Planet models, depending on which two planets are
modeled. The phase-folded plots for these three planets are
shown in Figure 9 in the Appendix. The periods and velocity
semiamplitudes ($K_b = 0.454 \pm 0.060\,\mathrm{m\,s^{-1}}$, $K_d = 0.479 \pm$
$0.058\,\mathrm{m\,s^{-1}}$, and $K_c = 0.467 \pm 0.058\,\mathrm{m\,s^{-1}}$) derived from the
analysis of the MAROON-X Red arm data for all three signals
are consistent with the results of J. I. González Hernández et al.
(2024) within 1.5σ. Therefore, we confirm planet b and planet
candidates c and d independently using MAROON-X alone.

Additionally, although the periodogram of the 3-Planet model
does not show any significant signal, it shows some power
around the period of planet candidate e ($P = 6.739$ days). A four-
planet fit centered at this period provides a comparable value for
the marginal evidence with the solution converging to same
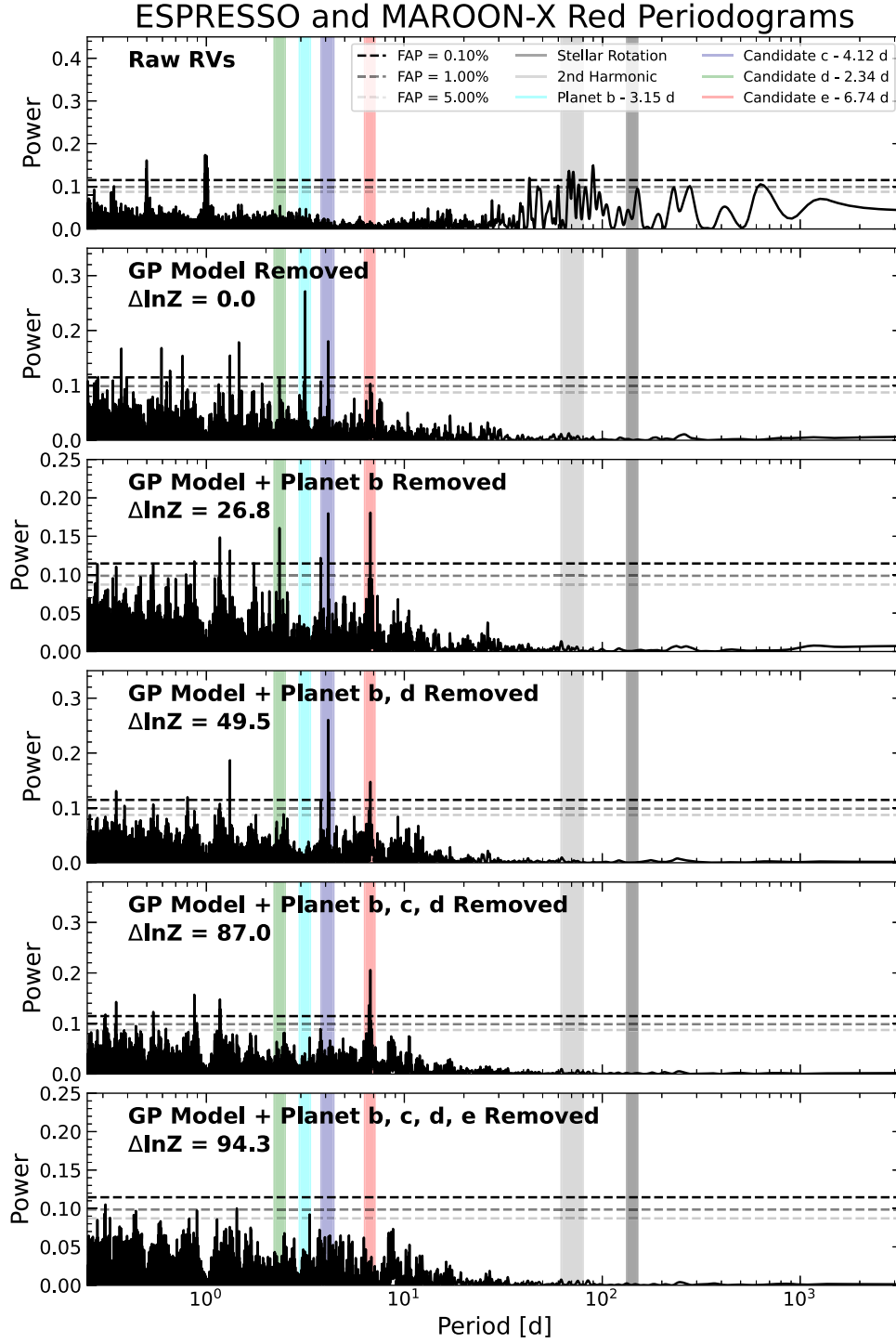period as identified by J. I. González Hernández et al. (2024).

Figure 2. This plot shows the computed GLS periodograms for the combined residuals of MAROON-X Red channel and ESPRESSO radial velocities. A β distribution for the planetary eccentricities has been used for all planets.

3.3. Joint Analysis of MAROON-X and ESPRESSO

Given the consistency of our results compared to J. I. González Hernández et al. (2024), we then turned our attention to joint modeling of the MAROON-X and ESPRESSO data to further constrain the system. We adopted the 149 radial velocities (which were derived via the S-BART code; A. M. Silva et al. 2022) of the ESPRESSO data from J. I. González Hernández et al. (2024). Joint periodograms of the MAROON-X Red arm ESPRESSO radial velocities with

successive planet signals removed are shown in Figure 2. The evidence for each model is given in Table 2.

We ran the 4-Keplerian model 10 times to analyze any variance in marginal evidence. The $\ln Z$ ranges between $[-328.7, -320.3]$ with a median and standard deviation of -325.6 ± 2.6. The posteriors are consistent within different runs. However, for the 4-Keplerian model, the runs with the lowest $\ln Z$ have a slightly larger scatter ($<0.03\%$ of the samples) outside the period range 6.72–6.76 in comparison to the fit with the highest marginal evidence ($<0.005\%$ of the

samples). We identify this as the major source of the observed variance in ln Z. We report the median values of ln Z in Table 2 and in Figure 2, and we select the model with evidence closest to the median ln Z value as our final model.

The signals for planets b, c, and d show up clearly in the periodograms, and models with increasing planet numbers have very large improvements in the evidence. Furthermore, the signal for planet candidate e in the periodogram is strengthened compared to the ESPRESSO-only results (FAP = 10^{-7}% versus 2%), and the change in evidence between the 3- and 4-Planet models is highly significant ($\Delta \ln Z = 7.3$). We therefore also consider planet candidate e confirmed as a bona fide planet.

The final parameters for the 4-Planet model are given in Table 3, the phase-folded velocities are shown in Figure 3, and the instrumental parameters are provided in Table 5 in the Appendix. The corner plot with 20 planetary parameters and six GP hyperparameters is shown in Figure 14 in the Appendix. No further significant peaks are seen in the combined MAROON-X Red channel and ESPRESSO residuals after subtracting the 4-Planet model. We also repeated this analysis for a global GP model where the stellar activity is modeled under a common covariance matrix. All parameters are in excellent agreement with the instrument-by-instrument GP model. The median values of ln Z for different global GP models are presented in Table 2, while the realized GP for the 4-Keplerian model is shown in Figure 7 in the Appendix.

3.4. Stability Analysis

Our proposed four-planet configuration for Barnard's Star is remarkably compact (see discussion in Section 4), thus raising the question of whether such a system would be stable. We investigated this by using the SPOCK tool (D. Tamayo et al. 2020) and numerical integrations using the REBOUND code (H. Rein & S. F. Liu 2012). SPOCK is an algorithm that uses machine learning and resonant dynamics to assess the probability of dynamical stability of compact systems with three to five planets.

We found that our best-fit point estimate for the planets' parameters results in an unstable system within 2000 yr. When mapping the parameter space, we found that the small, but nonzero, eccentricities of the planets in the best-fit solution are likely to blame for this instability. Using SPOCK, we see that the system has a <80% chance of being stable if any one of the planets besides e has $e > 0.02$, even when all the others have $e = 0$.

Motivated by these results, we ran a joint MAROON-X +ESPRESSO fit with the eccentricities fixed to zero. The best-fit eccentricities in Table 3 are all consistent with zero within 1.5σ. The evidence is somewhat higher for the nonzero eccentricity fit ($\Delta \ln Z = 1.2$), but there is a known bias to nonzero eccentricity in radial velocity fits (G. Laughlin et al. 2005).

We found that the four-planet system remains stable over 10^9 orbits of the shortest-period planet ($P = 2.340$ days) when zero eccentricities are assumed for all the planets. This holds true for planet masses up to 3 times the values given in Table 3, meaning that the system is stable for planet inclinations ranging from 20° to 90°. Even in cases of low inclination, SPOCK returns an over 90% probability that the system is stable. We therefore conclude that our proposed four-planet configuration is not obviously unstable and that eccentricities <0.02 are

Table 3
This Table Summarizes the Posteriors and the Priors for the Four Planets as Derived from a Joint Fit between MAROON-X Red Channel and ESPRESSO Radial Velocities

Planetary Parameters		
Parameter	Posterior	Prior distribution
P_d (days)	$2.3402^{+0.0003}_{-0.0003}$	$\mathcal{U}[2.29, 2.39]$
$t_{0,d}$ (BJD—2450000)	$10243.70^{+0.08}_{-0.07}$	$\mathcal{U}[10242.54, 10244.89]$
K_d (m s^{-1})	$0.428^{+0.036}_{-0.036}$	$\mathcal{U}[0, 2]$
e_d	$0.04^{+0.05}_{-0.03}$	$\beta[1.52, 29.0]$
ω_d (deg)	$-51.8^{+190.8}_{-93.5}$	$\mathcal{U}[-180, 180]$
$m_d \sin i_d$ ($M_\oplus$)	0.263 ± 0.024	⋯
a_d (au)	0.0188 ± 0.0003	⋯
$T_{eq,d}$ (K)[a]	483	⋯
P_b (days)	$3.1542^{+0.0004}_{-0.0004}$	$\mathcal{U}[3.1, 3.2]$
$t_{0,b}$ (BJD—2450000)	$10243.38^{+0.09}_{-0.09}$	$\mathcal{U}[10242.12, 10245.32]$
K_b (m s^{-1})	$0.440^{+0.036}_{-0.036}$	$\mathcal{U}[0, 2]$
e_b	$0.03^{+0.03}_{-0.02}$	$\beta[1.52, 29.0]$
ω_b (deg)	$+3.8^{+117.7}_{-121.4}$	$\mathcal{U}[-180, 180]$
$m_b \sin i_b$ ($M_\oplus$)	0.299 ± 0.026	⋯
a_b (au)	0.0229 ± 0.0003	⋯
$T_{eq,b}$ (K)[a]	438	⋯
P_c (days)	$4.1244^{+0.0006}_{-0.0006}$	$\mathcal{U}[4.07, 4.17]$
$t_{0,c}$ (BJD—2450000)	$10242.92^{+0.10}_{-0.10}$	$\mathcal{U}[10241.62, 10245.82]$
K_c (m s^{-1})	$0.452^{+0.038}_{-0.038}$	$\mathcal{U}[0, 2]$
e_c	$0.08^{+0.06}_{-0.05}$	$\beta[1.52, 29.0]$
ω_c (deg)	$90.8^{+38.9}_{-48.1}$	$\mathcal{U}[-180, 180]$
$m_c \sin i_c$ ($M_\oplus$)	0.335 ± 0.030	⋯
a_c (au)	0.0274 ± 0.0004	⋯
$T_{eq,c}$ (K)[a]	400	⋯
P_e (days)	$6.7392^{+0.0028}_{-0.0028}$	$\mathcal{U}[6.69, 6.79]$
$t_{0,e}$ (BJD—2450000)	$10245.30^{+0.37}_{-0.36}$	$\mathcal{U}[10240.32, 10247.12]$
K_e (m s^{-1})	$0.221^{+0.037}_{-0.037}$	$\mathcal{U}[0, 2]$
e_e	$0.04^{+0.04}_{-0.03}$	$\beta[1.52, 29.0]$
ω_e (deg)	$-27.5^{+137.5}_{-96.1}$	$\mathcal{U}[-180, 180]$
$m_e \sin i_e$ ($M_\oplus$)	0.193 ± 0.033	⋯
a_e (au)	0.0381 ± 0.0005	⋯
$T_{eq,e}$ (K)[a]	340	⋯
GP hyperparameters		
σ_{GP-ESP}	$1.98^{+0.28}_{-0.22}$	$\mathcal{U}[0, 10]$
$\sigma_{GP-MXRed}$	$1.78^{+0.45}_{-0.33}$	$\mathcal{U}[0, 10]$
$GP - P_{rot}$	$140.99^{+8.27}_{-8.41}$	$\mathcal{N}[142, 9]$
$GP - Q0$	$0.37^{+0.39}_{-0.21}$	$\mathcal{LU}[0.1, 6]$
$GP - f$	$0.72^{+0.20}_{-0.30}$	$\mathcal{U}[0, 1]$
$GP - dQ$	$0.25^{+0.44}_{-0.12}$	$\mathcal{LU}[0.1, 25]$

Note.
[a] T_{eq} is calculated assuming zero albedo and full heat redistribution.

favored. Nevertheless, a more detailed analysis of the system's stability is warranted.

3.5. Limits on the Habitable Zone

Based on the calculations of R. K. Kopparapu et al. (2013, 2014), the habitable zone of Barnard's Star corresponds to orbital periods of 10–42 days assuming a 1 $M_\oplus$ planet. The four detected planets are all closer to the star than the inner edge of the habitable zone, and there is no evidence of signals at longer
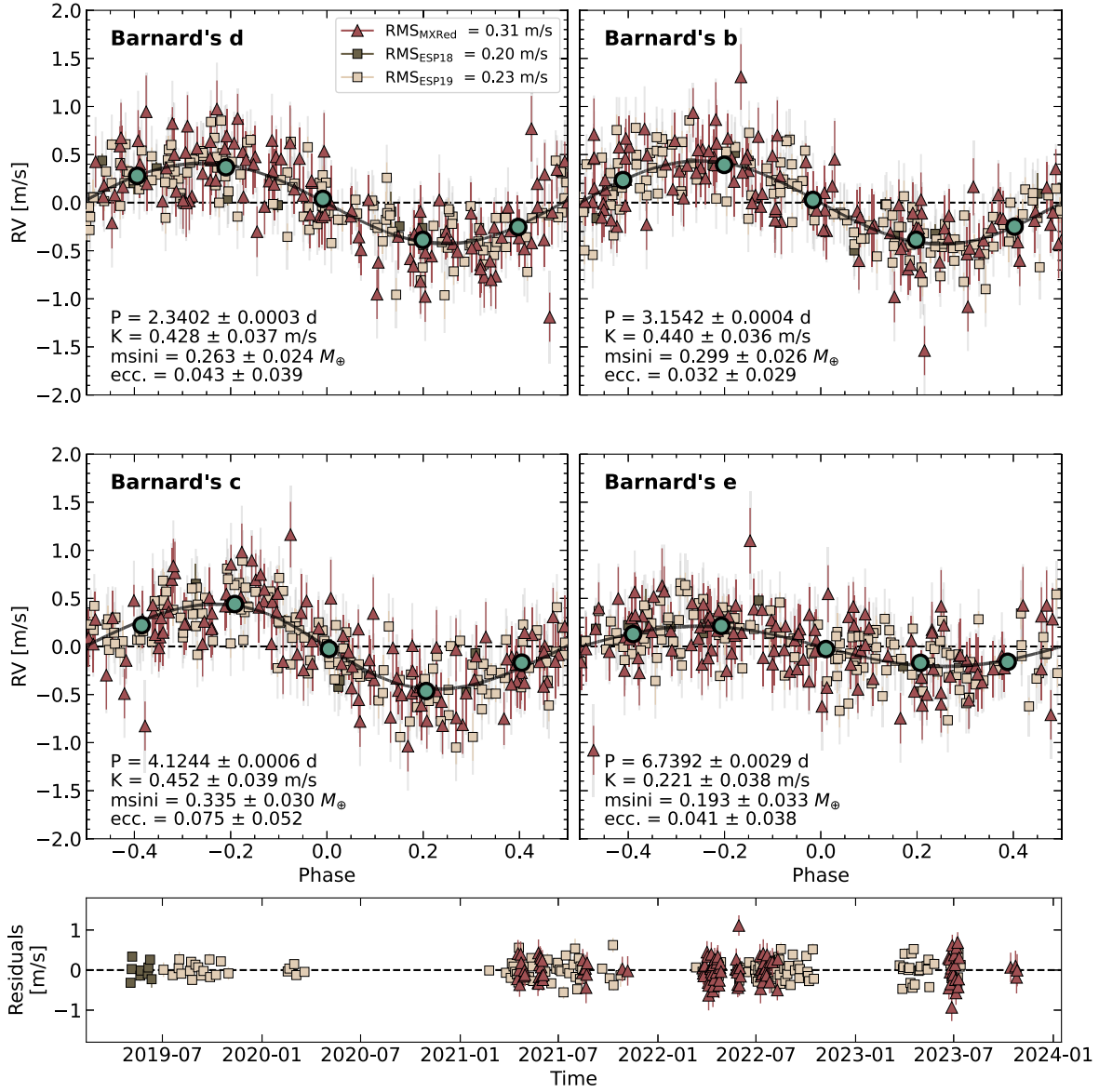
Figure 3. Top panels: phase-folded plots for planets Barnard b, c, d, and e based on joint fit between MAROON-X Red channel and ESPRESSO radial velocities. Bottom panel: residuals as a function of time for the 4-Planet model.

periods. We therefore used the data to place limits on additional planets in the system.

We performed a suite of injection-recovery tests on the residuals of our four-planet joint fit of MAROON-X Red channel and ESPRESSO data using `rvsearch` (L. J. Rosenthal et al. 2021). We injected 10,000 planetary signals where the semiamplitudes, orbital periods, argument of periastron, and time of periastron passage were drawn from a uniform distribution while the eccentricities were drawn from a β distribution following D. M. Kipping (2013). A planetary signal is classified as recovered if `rvsearch` recovered the orbital period and semiamplitude within 25% of the true values.

The results of our injection-recovery test are shown in Figure 4. A similar analysis on the residuals of the four-planet fit to the ESPRESSO-only data set reveals the detection probability of a planet e analog (with parameters from Table 3) to be 59%. The detection probability of planet e in the residuals of the joint fit between MAROON-X Red channel and ESPRESSO data improves to 79%, thus making the detection
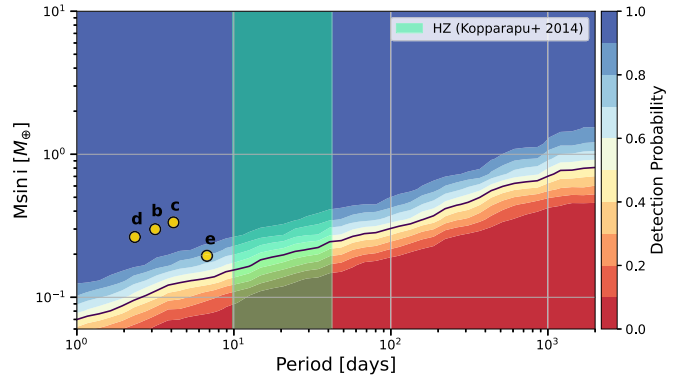
Figure 4. This plot shows the current sensitivity of detecting planets around Barnard's Star using the MAROON-X Red channel and ESPRESSO data.

of planet e more likely with the combined data set. Based on our analysis, the current measurements allow us to rule out the presence of planets with minimum masses 0.37–$0.57 M_{\oplus}$
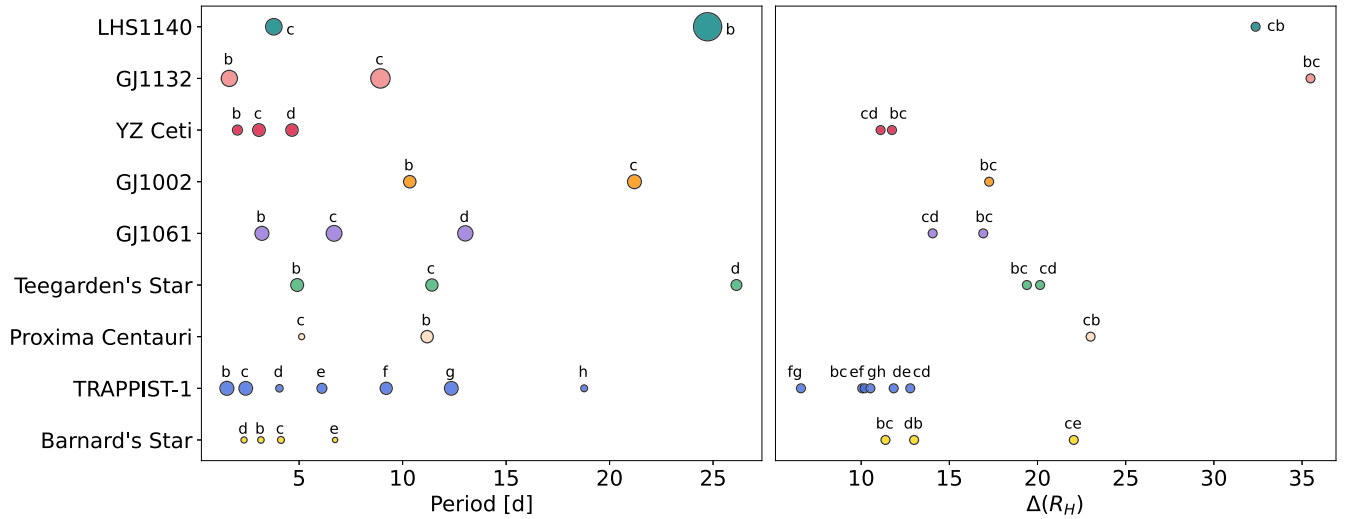
Figure 5. This plot shows a comparison of planetary architectures between Barnard's Star and other compact M dwarf systems. Left panel: orbital periods of different planets with symbol sizes proportional to the planets' masses. Right panel: mutual Hill separations between consecutive planets in the systems.

(detection probability >0.99) near the inner and outer edges of the habitable zone. Further observations are needed to investigate the presence of planets with even lower masses.

4. Discussion

At long last Barnard's Star has planets confirmed with two different instruments. Demonstrating the power of this new generation of EPRV spectrographs, the planet signals are all $<50\,\mathrm{cm\,s^{-1}}$, and the planets have minimum masses $<0.34\,M_\oplus$. Barnard e is in contention with Proxima d (J. P. Faria et al. 2022) as the lowest-mass planet detected with radial velocities ($m\sin i = 0.19 \pm 0.03\,M_\oplus$ versus $0.26 \pm 0.05\,M_\oplus$, respectively). With $K = 0.221 \pm 0.038\,\mathrm{cm\,s^{-1}}$, Barnard e has the lowest radial velocity semiamplitude of a claimed planet. We measure this signal to 6σ confidence using MAROON-X and ESPRESSO.

The Barnard's Star system is remarkably compact. S. Dreizler et al. (2024) compared the values of mutual Hill radius separation ($\Delta(R_H)$) of several multiplanetary systems hosted by late M dwarfs that consisted of at least one potential rocky planet ($<2\,M_\oplus$). In this study, we conduct a similar analysis, incorporating Barnard's Star into the comparison. The left panel of Figure 5 compares the planets orbiting Barnard's Star to those in eight other compact multiplanet systems: (1) TRAPPIST-1 (E. Agol et al. 2021), (2) GJ 1132 (X. Bonfils et al. 2018; Q. Xue et al. 2024), (3) YZ Ceti (S. Stock et al. 2020), (4) GJ 1002 (A. Suárez Mascareño et al. 2023), (5) GJ 1061 (S. Dreizler et al. 2020), (6) Teegarden's Star (S. Dreizler et al. 2024), (7) Proxima Centauri (J. P. Faria et al. 2022), and (8) LHS 1140 (C. Cadieux et al. 2024). The marker sizes scale with the minimum mass (or actual mass for TRAPPIST-1 planets and GJ 1132b). The right panel illustrates the mutual Hill radius separations for consecutive planets across all nine systems. The inner three planets orbiting Barnard's Star have comparable separations as the compact TRAPPIST-1 and YZ Ceti systems. As described in Section 3.4, we find that the eccentricities of the Barnard's Star planets are all consistent with zero, thus likely aiding the dynamical stability of the system.

The radial velocity data for Barnard's Star show remarkably low scatter after just removing a simple model for rotationally modulated activity. The MAROON-X Red channel residuals have an rms of $31\,\mathrm{cm\,s^{-1}}$, which is essentially equivalent to their average photon-limited errors of $29\,\mathrm{cm\,s^{-1}}$. The ESPRESSO residuals have an rms of $24\,\mathrm{cm\,s^{-1}}$, which is substantially larger than their typical uncertainties of $10\,\mathrm{cm\,s^{-1}}$. This could either be indicative of residual stellar activity or unidentified instrument systematics. Our experience with MAROON-X and our take-aways from the literature suggest that even the best EPRV instruments are still not achieving their maximum potential performance. For example, neither the MAROON-X data nor the ESPRESSO data were based on laser frequency comb calibration, and both instruments experience variations in temperature and pressure that could be controlled better. The detection of such small planets with large, but not overly intensive, data sets obtained with suboptimal instrument performance bodes well for the future of radial velocity planet searches. It is remarkable that radial velocities can still push the frontier of exoplanet detection even 30 yr after the detection of 51 Peg b (M. Mayor & D. Queloz 1995).

Appendix

This Appendix contains the radial velocity data and supplementary figures (Tables 4 and 5, Figures 6–14).

Table 4
MAROON-X Radial Velocity (RV) Data Set of Barnard's Star

BJD (days)	RV MX Red (m s^{-1})	Error MX Red (m s^{-1})	RV MX Blue (m s^{-1})	Error MX Blue (m s^{-1})
2459321.089339	−8.48	0.32	−7.64	0.42
2459322.110600	−9.66	0.34	−8.33	0.46
2459324.112461	−10.01	0.29	−9.16	0.37
2459325.114176	−8.75	0.30	−8.45	0.38
2459327.100589	−9.50	0.32	−8.04	0.41
2459328.109813	−8.67	0.36	−8.03	0.50
2459333.007912	−8.23	0.32	−5.83	0.43
2459333.969222	−7.70	0.30	−6.44	0.40
2459335.009764	−7.07	0.28	−5.93	0.35
2459358.965661	−5.06	0.33	−4.74	0.50
2459359.919573	−6.34	0.34	−4.71	0.52
2459360.121373	−5.67	0.19	−4.30	0.29
2459361.030219	−6.50	0.34	−4.18	0.51
2459361.948153	−7.03	0.28	−5.38	0.39
2459362.979858	−6.01	0.25	−4.83	0.31
2459363.944908	−7.38	0.26	−5.46	0.36
2459365.032154	−7.05	0.24	−6.18	0.31
2459366.047448	−6.26	0.19	−4.84	0.26
2459367.114880	−6.87	0.26	−5.17	0.40
2459368.008443	−5.47	0.27	−4.09	0.36
2459368.907788	−6.57	0.25	−5.42	0.35
2459440.742736	−4.98	0.30	−3.94	0.38
2459441.799269	−5.09	0.28	−3.48	0.33
2459444.906483	−4.60	0.29	−3.60	0.41
2459446.781749	−5.08	0.34	−4.04	0.45
2459447.847732	−4.05	0.39	−2.76	0.58
2459448.775678	−5.15	0.22	−2.98	0.34
2459449.826562	−4.25	0.27	−3.59	0.32
2459514.722096	−1.70	0.31	0.20	0.46
2459524.690827	−1.19	0.37	1.10	0.57
2459663.045448	0.97	0.29	2.96	0.47
2459664.139126	0.89	0.27	−0.90	0.39
2459665.034895	2.31	0.22	0.26	0.28
2459666.144693	0.04	0.25	1.24	0.32
2459667.130997	0.42	0.28	1.75	0.39
2459671.144615	0.84	0.27	2.73	0.36
2459672.030593	2.38	0.19	1.30	0.26
2459673.141590	1.60	0.27	2.47	0.36
2459674.020896	2.12	0.21	3.21	0.30
2459674.148511	2.52	0.38	3.43	0.57
2459678.001730	2.19	0.30	3.35	0.40
2459678.094617	2.18	0.29	4.68	0.39
2459679.038478	1.58	0.30	3.47	0.41
2459679.139257	1.96	0.31	4.70	0.43
2459681.016456	2.85	0.18	5.21	0.27
2459681.139209	3.17	0.35	5.27	0.51
2459682.034007	2.38	0.40	4.52	0.62
2459682.981733	0.87	0.30	2.91	0.40
2459683.106694	1.62	0.33	2.56	0.45
2459684.140664	3.03	0.29	5.72	0.36
2459685.135344	1.66	0.29	3.32	0.36
2459687.984864	1.47	0.19	2.98	0.29
2459689.029985	1.05	0.32	2.72	0.44
2459690.124045	1.29	0.28	3.12	0.33
2459691.105625	1.09	0.29	3.22	0.34
2459693.070956	2.22	0.32	3.99	0.41
2459693.950918	1.56	0.25	3.51	0.37

Table 4
(Continued)

| BJD (days)	RV MX Red (m s^{-1})	Error MX Red (m s^{-1})	RV MX Blue (m s^{-1})	Error MX Blue (m s^{-1})
2459695.097745	0.15	0.29	1.88	0.35
2459696.065464	0.52	0.29	2.00	0.35
2459697.014077	1.62	0.29	2.73	0.35
2459724.013139	3.87	0.25	2.30	0.33
2459725.131552	4.41	0.27	3.15	0.37
2459726.013637	5.31	0.25	3.42	0.33
2459726.937287	3.86	0.24	1.76	0.31
2459727.934069	4.72	0.32	2.87	0.44
2459728.100608	4.96	0.17	3.24	0.23
2459729.935123	3.18	0.26	1.53	0.32
2459730.924961	5.78	0.26	3.38	0.34
2459731.896371	4.32	0.25	2.34	0.33
2459733.036065	4.41	0.18	2.87	0.24
2459768.885438	1.56	0.30	0.26	0.40
2459768.982170	1.84	0.34	−0.30	0.49
2459769.974648	2.78	0.36	0.24	0.53
2459770.900837	2.23	0.28	−0.64	0.36
2459771.868236	2.37	0.25	−0.00	0.30
2459772.000134	2.68	0.29	−0.01	0.37
2459772.922860	2.56	0.29	0.86	0.38
2459774.016654	0.56	0.32	−0.39	0.50
2459774.972000	1.25	0.36	0.24	0.50
2459775.811500	1.53	0.27	−1.82	0.33
2459778.846142	0.95	0.32	−1.93	0.42
2459779.979551	1.26	0.31	−1.56	0.40
2459780.916053	-0.18	0.29	−3.44	0.36
2459781.977301	0.19	0.30	−2.71	0.38
2459786.869912	0.56	0.28	−2.63	0.34
2459787.762706	0.24	0.28	−3.73	0.34
2459791.955902	1.73	0.35	−2.12	0.47
2459800.964511	4.20	0.26	0.56	0.41
2459801.819144	1.65	0.21	−1.34	0.31
2460116.920705	5.74	0.19	4.25	0.27
2460117.873013	5.33	0.28	3.11	0.37
2460118.934507	5.61	0.26	4.14	0.31
2460119.787149	5.11	0.25	3.49	0.31
2460120.882366	5.12	0.27	3.79	0.35
2460121.891302	5.66	0.30	4.27	0.42
2460123.001395	6.45	0.34	5.27	0.49
2460124.007448	3.67	0.26	2.54	0.34
2460124.931171	3.65	0.19	2.36	0.25
2460125.945157	5.42	0.38	4.44	0.56
2460127.982584	3.29	0.27	2.07	0.33
2460129.017544	4.03	0.36	3.87	0.51
2460129.908421	3.88	0.16	1.87	0.22
2460130.833025	4.41	0.30	1.67	0.39
2460131.845693	2.22	0.26	0.57	0.32
2460133.951563	1.75	0.26	0.12	0.31
2460134.864425	4.09	0.20	2.01	0.28
2460135.825284	3.53	0.22	1.85	0.31
2460136.794707	1.22	0.30	−0.32	0.39
2460231.740856	12.38	0.37	9.49	0.47
2460240.753485	13.15	0.39	10.64	0.53
2460242.699704	14.68	0.40	11.10	0.54
2460243.718891	13.09	0.40	10.14	0.55
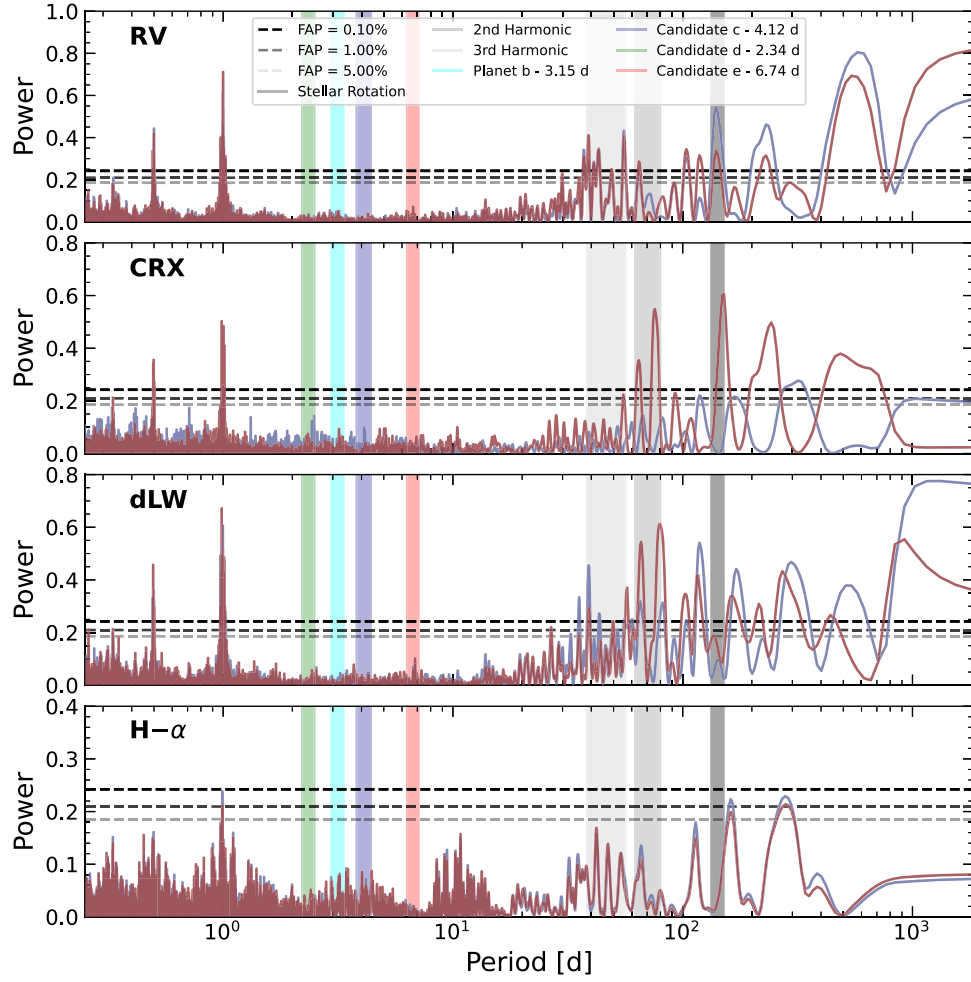
Figure 6. This plot shows the computed GLS periodograms of raw radial velocities (red color for Red channel data and blue color for Blue channel data, chromatic index (CRX), differential line widths (dLW), and Hα index for MAROON-X Red and Blue channel data.
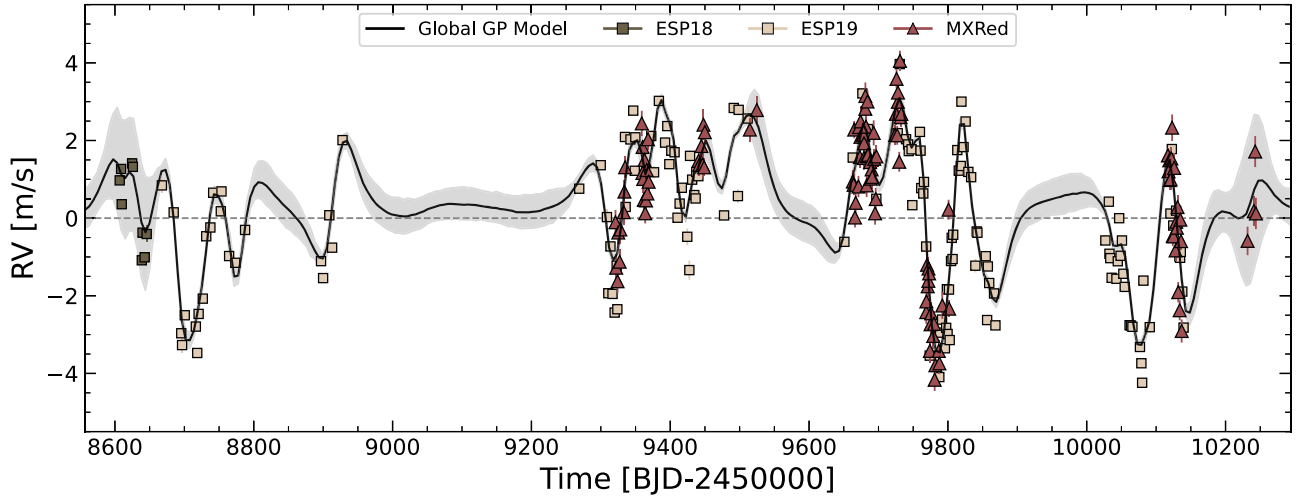

Figure 7. This plot shows the global GP model for the 4-Keplerian model joint fit between the MAROON-X Red channel and ESPRESSO data sets.
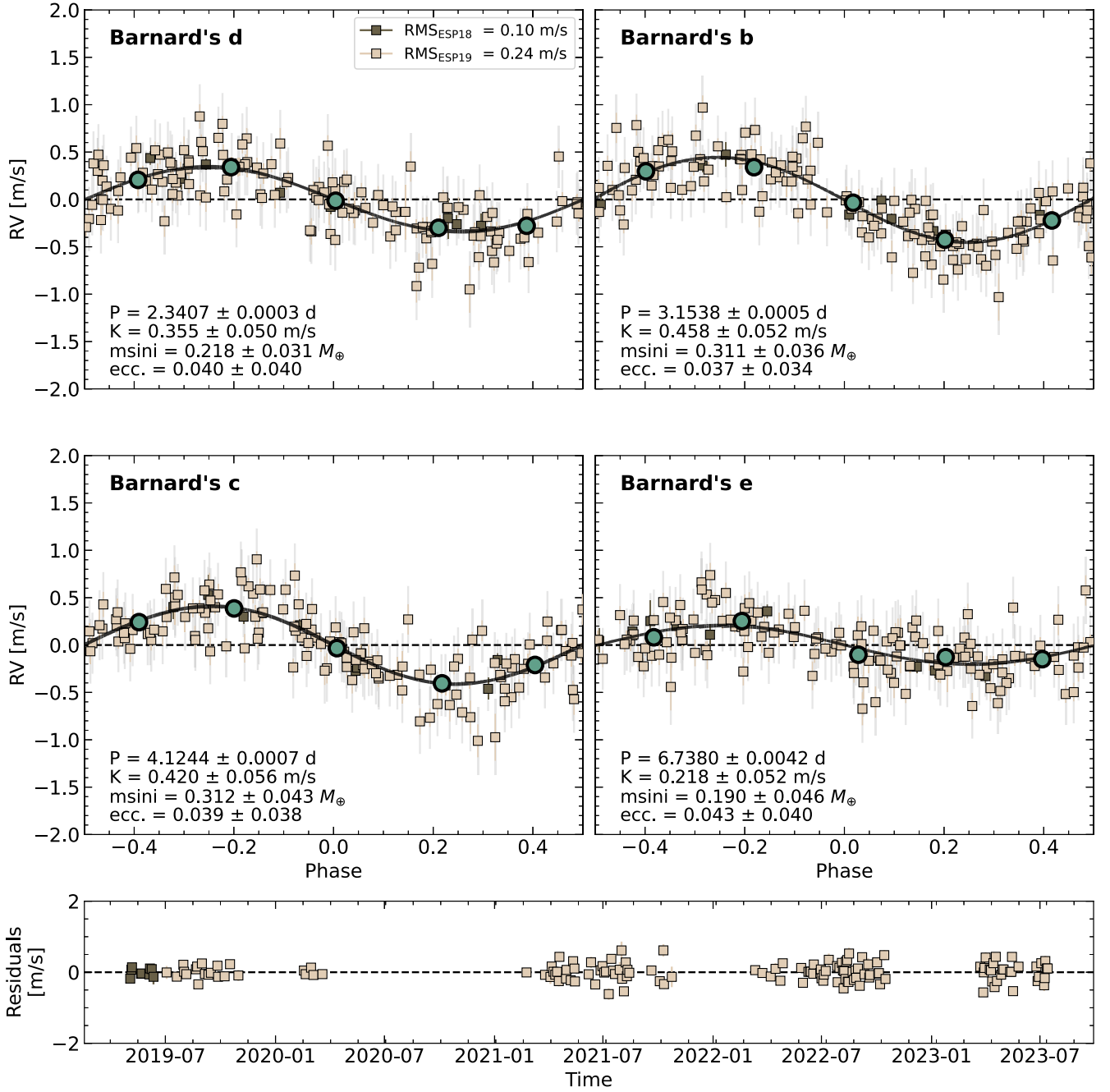
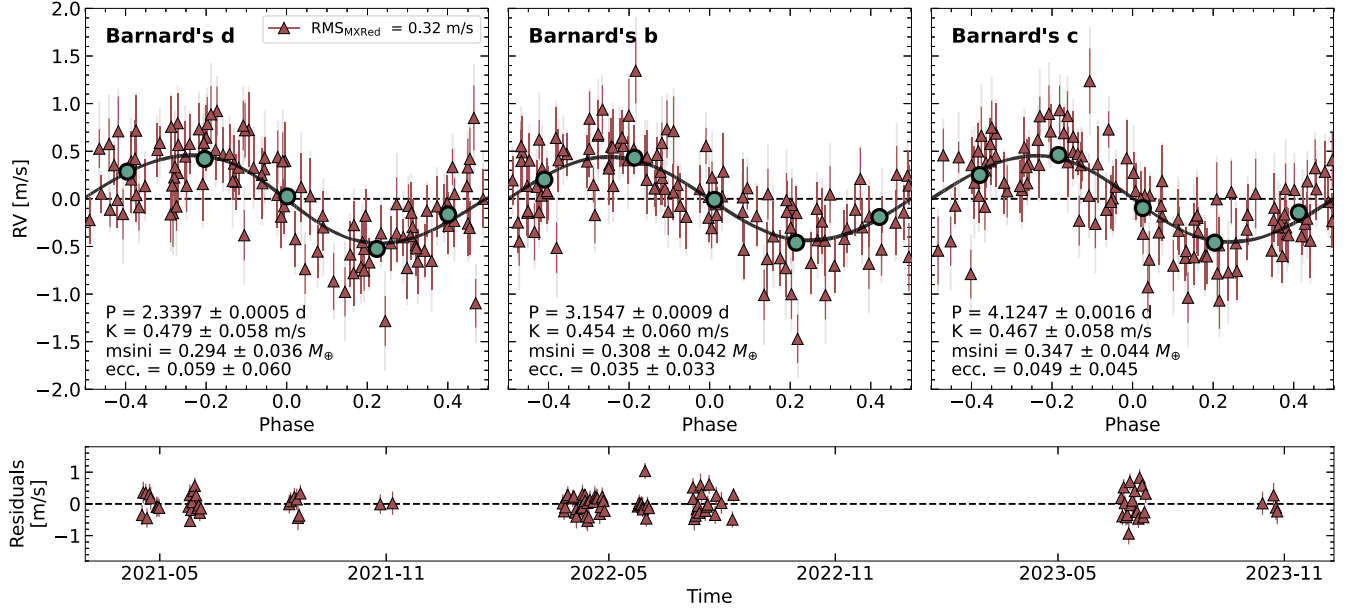**Figure 8.** Phase-folded plots for planets Barnard b, c, d, and e using ESPRESSO data.

Barnard's d

P = 2.3407 ± 0.0003 d
K = 0.355 ± 0.050 m/s
msini = 0.218 ± 0.031 $M_\oplus$
ecc. = 0.040 ± 0.040

Barnard's b

P = 3.1538 ± 0.0005 d
K = 0.458 ± 0.052 m/s
msini = 0.311 ± 0.036 $M_\oplus$
ecc. = 0.037 ± 0.034

Barnard's c

P = 4.1244 ± 0.0007 d
K = 0.420 ± 0.056 m/s
msini = 0.312 ± 0.043 $M_\oplus$
ecc. = 0.039 ± 0.038

Barnard's e

P = 6.7380 ± 0.0042 d
K = 0.218 ± 0.052 m/s
msini = 0.190 ± 0.046 $M_\oplus$
ecc. = 0.043 ± 0.040

RMS$_{ESP18}$ = 0.10 m/s
RMS$_{ESP19}$ = 0.24 m/s

Figure 9. Phase-folded plots for planets Barnard b, c, and d based on MAROON-X Red Channel data. The bottom panel shows the residuals of the 3-Planet model for MAROON-X Red channel radial velocities.
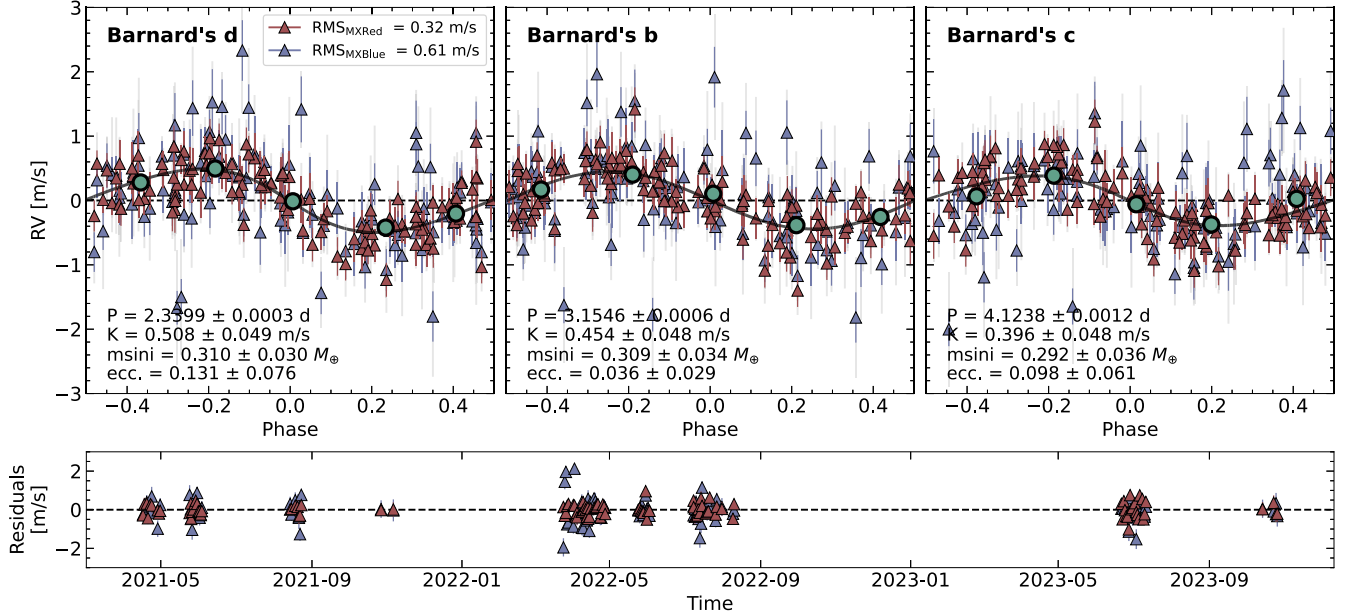
Figure 10. Phase-folded plots for planets Barnard b, c, d, and e based on joint fit between MAROON-X Red and Blue channel radial velocities.
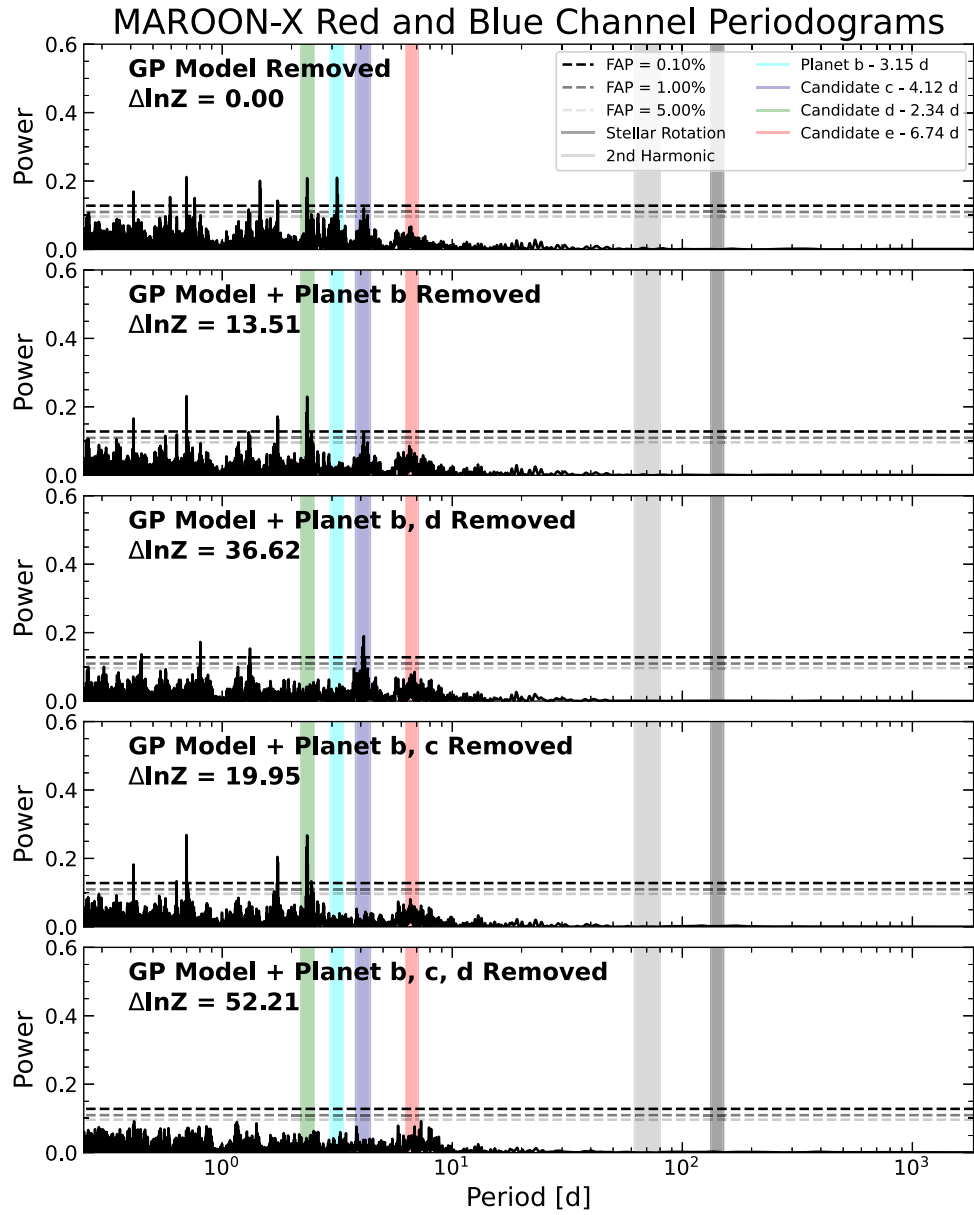
Figure 11. This plot shows the computed GLS periodograms for the combined residuals of MAROON-X Red and Blue channel radial velocities. A β distribution for the planetary eccentricities has been used for all planets.
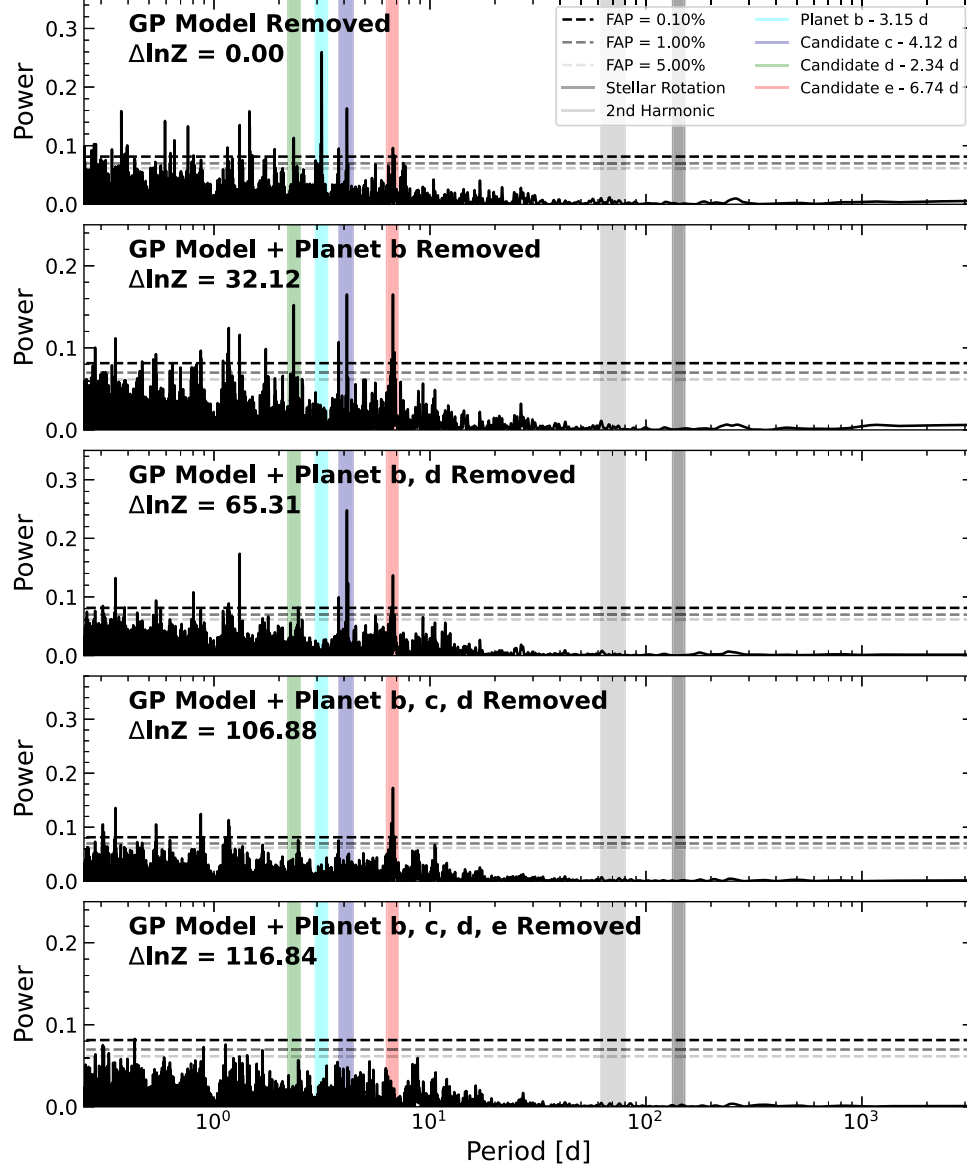
Figure 12. This plot shows the computed GLS periodograms for the combined residuals of MAROON-X Red channel, Blue channel, and ESPRESSO radial velocities. A β distribution for the planetary eccentricities has been used for all planets.
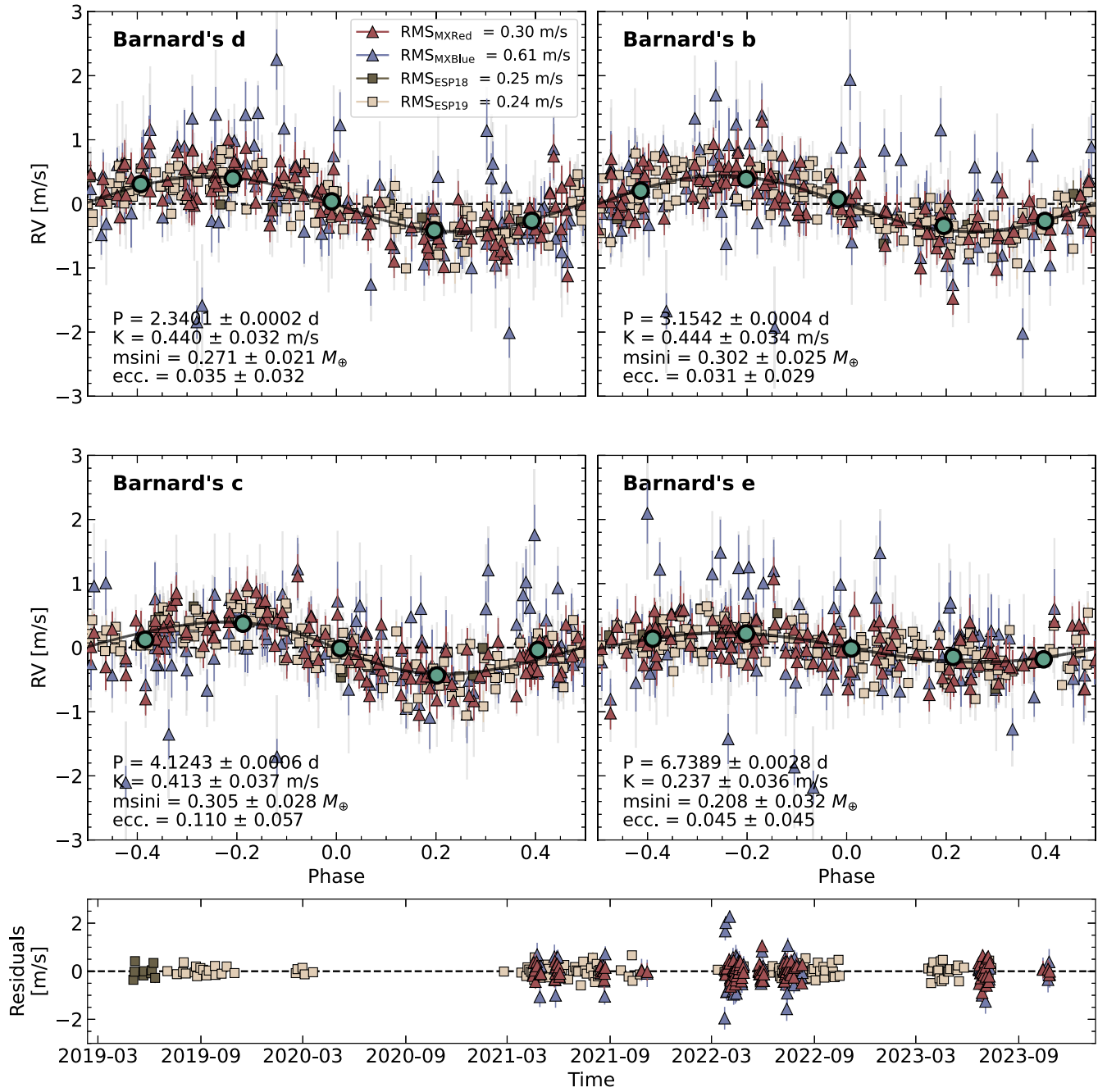
Figure 13. Phase-folded plots for planets Barnard b, c, d, and e based on joint fit between MAROON-X Red channel, Blue channel, and ESPRESSO radial velocities.
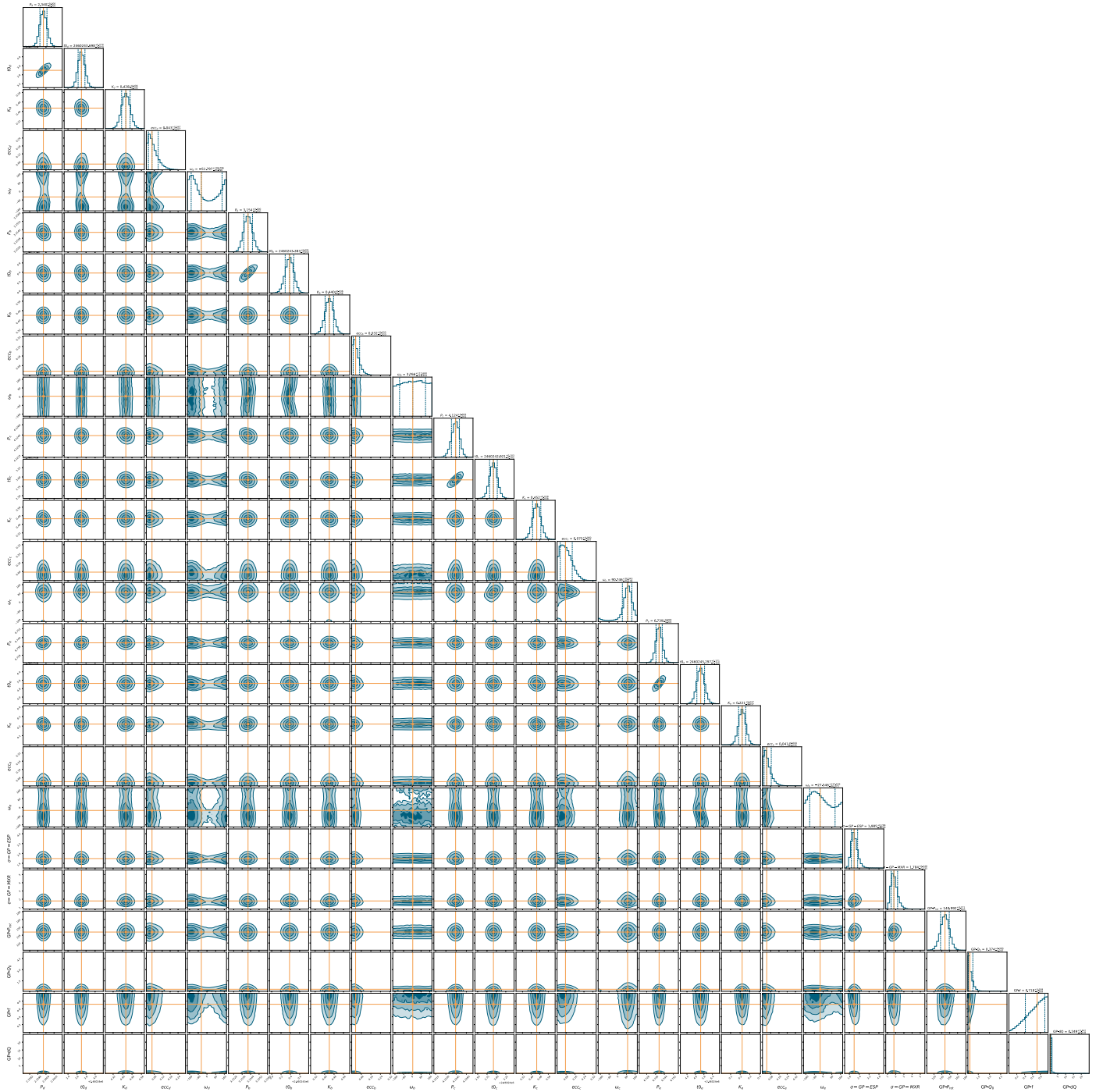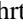
Figure 14. Corner plot for the four-planet joint fit to MAROON-X Red channel and ESPRESSO data sets. We only plot this for the 20 planetary parameters and six GP hyperparameters.

Table 5
This Table Summarizes the Posteriors and Priors for the Instrumental Parameters for the Final 4-Keplerian Joint Fit between MAROON-X and ESPRESSO Data Sets

Instrumental Parameters		
Parameter	Posterior	Prior Distribution
$\gamma_{\rm ESP18}$	$0.22^{+1.44}_{-1.45}$	$\mathcal{U}[-20, 20]$
$\gamma_{\rm ESP19}$	$0.19^{+0.36}_{-0.37}$	$\mathcal{U}[-20, 20]$
$\gamma_{\rm 2021\ Apr\text{-}MXRed}$	$-8.53^{+1.64}_{-1.65}$	$\mathcal{U}[-20, 20]$
$\gamma_{\rm 2021\ May\text{-}MXRed}$	$-5.63^{+1.70}_{-1.65}$	$\mathcal{U}[-20, 20]$
$\gamma_{\rm 2021\ Aug\text{-}MXRed}$	$-5.22^{+1.69}_{-1.72}$	$\mathcal{U}[-20, 20]$
$\gamma_{\rm 2021\ Nov\text{-}MXRed}$	$-1.66^{+1.85}_{-1.86}$	$\mathcal{U}[-20, 20]$
$\gamma_{\rm 2022\ Apr\text{-}MXRed}$	$1.00^{+1.31}_{-1.32}$	$\mathcal{U}[-20, 20]$
$\gamma_{\rm 2022\ May\text{-}MXRed}$	$4.45^{+1.69}_{-1.73}$	$\mathcal{U}[-20, 20]$
$\gamma_{\rm 2022\ Jul\text{-}MXRed}$	$2.62^{+1.37}_{-1.33}$	$\mathcal{U}[-20, 20]$
$\gamma_{\rm 2023\ Jul\text{-}MXRed}$	$3.89^{+1.52}_{-1.56}$	$\mathcal{U}[-20, 20]$
$\gamma_{\rm 2023\ Oct\text{-}MXRed}$	$13.35^{+1.71}_{-1.67}$	$\mathcal{U}[-20, 20]$
$\sigma_{\rm ESP18}$	$0.30^{+0.21}_{-0.13}$	$\mathcal{LU}[0.1, 5.0]$
$\sigma_{\rm ESP19}$	$0.30^{+0.03}_{-0.03}$	$\mathcal{LU}[0.1, 5.0]$
$\sigma_{\rm 2021\ Apr\text{-}MXRed}$	$0.19^{+0.14}_{-0.07}$	$\mathcal{LU}[0.1, 5.0]$
$\sigma_{\rm 2021\ May\text{-}MXRed}$	$0.19^{+0.12}_{-0.07}$	$\mathcal{LU}[0.1, 5.0]$
$\sigma_{\rm 2021\ Aug\text{-}MXRed}$	$0.18^{+0.14}_{-0.06}$	$\mathcal{LU}[0.1, 5.0]$
$\sigma_{\rm 2021\ Nov\text{-}MXRed}$	$0.39^{+0.91}_{-0.24}$	$\mathcal{LU}[0.1, 5.0]$
$\sigma_{\rm 2022\ Apr\text{-}MXRed}$	$0.16^{+0.07}_{-0.04}$	$\mathcal{LU}[0.1, 5.0]$
$\sigma_{\rm 2022\ May\text{-}MXRed}$	$0.41^{+0.18}_{-0.13}$	$\mathcal{LU}[0.1, 5.0]$
$\sigma_{\rm 2022\ Jul\text{-}MXRed}$	$0.17^{+0.09}_{-0.05}$	$\mathcal{LU}[0.1, 5.0]$
$\sigma_{\rm 2023\ Jul\text{-}MXRed}$	$0.38^{+0.13}_{-0.10}$	$\mathcal{LU}[0.1, 5.0]$
$\sigma_{\rm 2023\ Oct\text{-}MXRed}$	$0.23^{+0.27}_{-0.10}$	$\mathcal{LU}[0.1, 5.0]$

ORCID iDs

Ritvik Basant ● https://orcid.org/0000-0003-4508-2436
Rafael Luque ● https://orcid.org/0000-0002-4671-2957
Jacob L. Bean ● https://orcid.org/0000-0003-4733-6532
Andreas Seifahrt ● https://orcid.org/0000-0003-4526-3747
Madison Brady ● https://orcid.org/0000-0003-2404-2427
Lily L. Zhao ● https://orcid.org/0000-0002-3852-3590
Nina Brown ● https://orcid.org/0009-0003-1142-292X
Tanya Das ● https://orcid.org/0009-0005-1486-8374
Julian Stürmer ● https://orcid.org/0000-0002-4410-4712
David Kasper ● https://orcid.org/0000-0003-0534-6388
Rohan Gupta ● https://orcid.org/0009-0002-1141-5853
Guðmundur Stefánsson ● https://orcid.org/0000-0001-7409-5688

References

Agol, E., Dorn, C., Grimm, S. L., et al. 2021, PSJ, 2, 1
Artigau, É., Cadieux, C., Cook, N. J., et al. 2022, AJ, 164, 84
Basant, R., Das, T., Bean, J. L., et al. 2025, AJ, submitted
Benedict, G. F., McArthur, B., Chappell, D. W., et al. 1999, AJ, 118, 1086
Bonfils, X., Almenara, J. M., Cloutier, R., et al. 2018, A&A, 618, A142
Bowens-Rubin, R., Akana Murphy, J. M., Hinz, P. M., et al. 2023, AJ, 166, 260
Brady, M., Bean, J. L., Seifahrt, A., et al. 2024, AJ, 168, 67

Caballero, J. A., González-Álvarez, E., Brady, M., et al. 2022, A&A, 665, A120
Cadieux, C., Plotnykov, M., Doyon, R., et al. 2024, ApJL, 960, L3
Crockett, C. J., Mahmud, N. I., Prato, L., et al. 2012, ApJ, 761, 164
Czesla, S., Schröter, S., Schneider, C. P., et al., 2019 PyA: Python astronomy-related packages, Astrophysics Source Code Library, ascl:1906.010
Dreizler, S., Jeffers, S. V., Rodríguez, E., et al. 2020, MNRAS, 493, 536
Dreizler, S., Luque, R., Ribas, I., et al. 2024, A&A, 684, A117
Espinoza, N., Kossakowski, D., & Brahm, R. 2019, MNRAS, 490, 2262
Faria, J. P., Suárez Mascareño, A., Figueira, P., et al. 2022, A&A, 658, A115
Fischer, D. A., Anglada-Escude, G., Arriagada, P., et al. 2016, PASP, 128, 066001
Foreman-Mackey, D. 2018, RNAAS, 2, 31
Foreman-Mackey, D., Agol, E., Ambikasaran, S., & Angus, R. 2017, AJ, 154, 220
France, K., Duvvuri, G., Egan, H., et al. 2020, AJ, 160, 237
Fulton, B. J., Petigura, E. A., Blunt, S., & Sinukoff, E. 2018, PASP, 130, 044504
Gaia Collaboration, Brown, A. G. A., Vallenari, A., et al. 2021, A&A, 649, A1
Gatewood, G. D. 1995, Ap&SS, 223, 91
Gauza, B., Béjar, V. J. S., Rebolo, R., et al. 2015, MNRAS, 452, 1677
Gliese, W. 1957, MiARI, 8, 1
González Hernández, J. I., Suárez Mascareño, A., Silva, A. M., et al. 2024, A&A, 690, A79
Huélamo, N., Figueira, P., Bonfils, X., et al. 2008, A&A, 489, L9
Kanodia, S., & Wright, J. 2018, RNAAS, 2, 4
Kipping, D. M. 2013, MNRAS, 434, L51
Kopparapu, R. K., Ramirez, R., Kasting, J. F., et al. 2013, ApJ, 765, 131
Kopparapu, R. K., Ramirez, R. M., SchottelKotte, J., et al. 2014, ApJL, 787, L29
Laughlin, G., Marcy, G. W., Vogt, S. S., Fischer, D. A., & Butler, R. P. 2005, ApJL, 629, L121
Lubin, J., Robertson, P., Stefansson, G., et al. 2021, AJ, 162, 61
Mayor, M., & Queloz, D. 1995, Natur, 378, 355
Pepe, F., Cristiani, S., Rebolo, R., et al. 2021, A&A, 645, A96
Queloz, D., Henry, G. W., Sivan, J. P., et al. 2001, A&A, 379, 279
Rajpaul, V., Aigrain, S., Osborne, M. A., Reece, S., & Roberts, S. 2015, MNRAS, 452, 2269
Rein, H., & Liu, S. F. 2012, A&A, 537, A128
Reiners, A., Bean, J. L., Huber, K. F., et al. 2010, ApJ, 710, 432
Reiners, A., & Zechmeister, M. 2020, ApJS, 247, 11
Rosenthal, L. J., Fulton, B. J., Hirsch, L. A., et al. 2021, ApJS, 255, 8
Seifahrt, A., Bean, J. L., Kasper, D., et al. 2022, Proc. SPIE, 12184, 121841G
Seifahrt, A., Bean, J. L., Stürmer, J., et al. 2016, Proc. SPIE, 9908, 990818
Seifahrt, A., Bean, J. L., Stürmer, J., et al. 2020, Proc. SPIE, 11447, 114471F
Seifahrt, A., Stürmer, J., Bean, J. L., & Schwab, C. 2018, Proc. SPIE, 12184, 107026D
Silva, A. M., Faria, J. P., Santos, N. C., et al. 2022, A&A, 663, A143
Speagle, J. S. 2020, MNRAS, 493, 3132
Stefanov, A. K., González Hernández, J. I., Suárez Mascareño, A., et al. 2025, A&A, 693, L3
Stock, S., Kemmer, J., Reffert, S., et al. 2020, A&A, 636, A119
Stürmer, J., Seifahrt, A., Schwab, C., & Bean, J. L. 2017, JATIS, 3, 025003
Suárez Mascareño, A., González-Álvarez, E., Zapatero Osorio, M. R., et al. 2023, A&A, 670, A5
Tamayo, D., Cranmer, M., Hadden, S., et al. 2020, PNAS, 117, 18194
Toledo-Padrón, B., González Hernández, J. I., Rodríguez-López, C., et al. 2019, MNRAS, 488, 5145
Trifonov, T., Caballero, J. A., Morales, J. C., et al. 2021, Sci, 371, 1038
Trotta, R. 2008, ConPh, 49, 71
Van Eylen, V., Albrecht, S., Huang, X., et al. 2019, AJ, 157, 61
Winters, J. G., Cloutier, R., Medina, A. A., et al. 2022, AJ, 163, 168
Xue, Q., Bean, J. L., Zhang, M., et al. 2024, ApJL, 973, L8
Zechmeister, M., & Kürster, M. 2009, A&A, 496, 577
Zechmeister, M., Reiners, A., Amado, P. J., et al. 2018, A&A, 609, A12